J. Fluid Mech. (2024), *vol*. 999, A93, doi:10.1017/jfm.2024.751

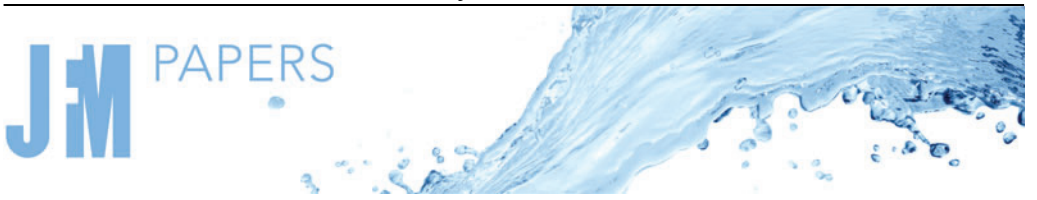

Experimental investigation of velocity and temperature distribution inside single droplet impingement on a heated substrate

Ruina Xu[1], **Gaoyuan Wang**[1], **Xun Zhu**[1] **and Peixue Jiang**[1],†

[1]Department of Energy and Power Engineering, Key Laboratory for Thermal Science and Power Engineering of Ministry of Education, Tsinghua University, Beijing 100084, PR China

(Received 4 September 2023; revised 9 June 2024; accepted 25 July 2024)

Droplet impingement on a heated substrate is the fundamental process underlying various technologies, ranging from spray cooling to inkjet printing. Understanding the coupled effects of fluid dynamics and heat transfer patterns during droplet jumping, boiling and evaporation, which determine the outcomes of the impingement process, is essential. Here, we developed two-colour planar laser-induced fluorescence and micro-particle image velocimetry technologies to measure quantitatively the velocity and temperature distributions inside the droplet during an impingement process with high temporal and spatial resolution. With our novel measuring system, the hot spots at the solid–liquid interface are discovered for the first time. The influence of contact boiling on the droplet internal mixing, which impedes droplet recoiling and reduces the rebounding velocity, is discussed. A significant enhancement in heat absorption for partially rebounding droplets is discovered, where the impingement heat transfer rate is doubled compared to other vapour-layer-covered droplets. The scaling correlations of viscous dissipation rate and contact time of rebounding droplets, as well as the time variation of droplet temperature rise, are proposed. More detailed patterns inside droplets can be captured by these experimental methods, which will help to reveal more intrinsic mechanisms lying in thermally induced flow, complex fluids and droplet-impacting-based technologies.

Key words: drops, multiphase flow, condensation/evaporation

1. Introduction

Droplet impingement commonly exists in nature and industrial processes, including spray cooling, spray coating and inkjet printing (Xu, Wang & Jiang 2021; Lohse 2022). Droplet impingement on a heated substrate differs significantly from that on a solid surface at

† Email address for correspondence: jiangpx@tsinghua.edu.cn

room temperature. The temperature difference between the solid surface and the liquid droplet not only elevates the fluid temperature, triggering more drastic phase changes (Benther *et al.* 2021; Yu *et al.* 2021), but also induces fluctuations and non-uniformities in fluid viscosity, density and surface tension (Cazabat & Guena 2010; Diddens, Li & Lohse 2021), resulting in more complex and diverse physical phenomena. Understanding of these phenomena is currently less comprehensive than that of droplet impingement on room-temperature substrates. Previous studies have investigated the effects of various factors such as fluid type, droplet diameter, impingement velocity and surface temperature on droplet impingement morphological characteristics (Wang, Lin & Cheng 2005; Tran *et al.* 2012; Staat *et al.* 2015; Chen *et al.* 2016; Shirota *et al.* 2016; Roisman, Breitenbach & Tropea 2018; Wang *et al.* 2022). The relative dominance between the heat transfer time scale and the flowing time scale varies with the impact parameters (Auliano *et al.* 2018), leading to different phenomena, including stick, spread, rebound, break-up, splash, boiling and evaporation (Moreira, Moita & Panão 2010; Lyu *et al.* 2019). The alterations in droplet macroscopic morphologies merely reflect the 'outcomes' of droplet impingement, while the underlying 'processes' that impact these outcomes through external factors are still unclear. Consequently, further exploration is necessary to understand the 'processes' involved in microscopic flow and heat transfer patterns.

When a droplet impinges onto a heated substrate, heat is transferred from the bottom to the top of the droplet, inducing a temperature gradient and internal convection, including Marangoni and Rayleigh convection (Bouillant *et al.* 2018; Diddens *et al.* 2021). Moreover, as the wall temperature rises, the evaporation behaviours and impact dynamics can be categorized into four regimes: evaporation, nucleate boiling, transition boiling and film boiling (Liang & Mudawar 2017). Within different boiling regimes, the processes of heat absorption and diffusion inside droplets vary, significantly affecting the cooling effect (Xu *et al.* 2021). It should be noted that the heat conduction and thermal convection patterns are influenced by both velocity and temperature fields. Therefore, further quantitative and simultaneous measurements on internal velocity and temperature distributions inside droplets are required to better understand the flow and heat transfer mechanisms.

As a well-developed method to study the internal flow inside droplets, micro-particle image velocimetry (μPIV) can provide a spatial resolution of a flow field down to several microns (Santiago *et al.* 1998; Stone, Stroock & Ajdari 2004) and has been utilized under various conditions, including evaporating droplets with single (Hamamoto, Christy & Sefiane 2011; Dash *et al.* 2014; Yim, Bouillant & Gallaire 2021) or multiple (Christy, Hamamoto & Sefiane 2011; Li *et al.* 2019; Efstratiou, Christy & Sefiane 2020; Diddens *et al.* 2021) components, Leidenfrost droplets with single (Bouillant *et al.* 2018; Yim *et al.* 2022; Yang *et al.* 2023) or multiple (Lyu *et al.* 2021) components, and droplets impacting onto heated surfaces (Lastakowski *et al.* 2014; Erkan 2019; Gultekin *et al.* 2020). Bouillant *et al.* (2018) studied the velocity field within quasi-static Leidenfrost droplets using μPIV. Their research revealed the self-rotation and self-propulsion phenomena of Leidenfrost droplets, which arise from an asymmetry in the vapour profile. Lyu *et al.* (2021) utilized μ PIV to study the internal flow of Ouzo Leidenfrost droplets, and revealed that the internal flow during emulsification was a result of thermocapillary flow and shear flow. As for the process of droplets impacting on a heated surface, Lastakowski *et al.* (2014) focused on the flow close to the substrate with bottom view μPIV. The radial velocity profile showed good agreement with inviscid convective flow theory (Roisman, Berberovı & Tropea 2009; Eggers *et al.* 2010). Gultekin *et al.* (2020) further studied the velocity profiles within single droplets or droplet pairs impacting on a heated substrate, and found that the radial profile is nonlinear outside due to capillary and viscous effects.

In recent years, temperature field measurement technologies such as infrared (IR) imaging (Shiri & Bird 2017; Teodori *et al.* 2018; Liu *et al.* 2022; Yim *et al.* 2022) and laser-induced fluorescence (LIF) thermometry (Chaze *et al.* 2017; Castanet *et al.* 2018, 2020) have been introduced to study the temperature distribution of droplets, providing new insights into micro-scale droplet heat transfer mechanisms. Chaze *et al.* (2017) employed two-colour LIF (2c-LIF) to investigate the temperature field inside a deionized water droplet impinging onto a 600 °C smooth surface with sampling frequency 15 Hz. They increased the resulting frequency by combining repeated experiments. The results indicated that increasing the droplet Weber number from 10 to 140 led to an increase in the average temperature rise from 15 °C to 40 °C. However, the reflection and refraction at the droplet interface may cause non-uniformity of laser intensity and add extra interference to the measurement results. They suggested that the application of 2c-LIF can improve the signal quality using the ratiometric principle. Additionally, they highlighted that the main challenges of droplet internal temperature field measurement include spectrum overlap, fluorescence attenuation, fluorescence self-excitation and total internal reflection. Castanet *et al.* (2018, 2020) examined water droplet impingement onto surfaces with temperatures ranging from 300 °C to 700 °C. Through theoretical and experimental studies, they demonstrated that the water temperature inside a Leidenfrost droplet can exceed the saturation temperature and reach the spinodal temperature, which is the highest temperature at which water can exist in a liquid state. For water at atmospheric pressure, the spinodal temperature is 320.25 °C.

Several previous researchers combined planar LIF (PLIF) with μPIV to realize the simultaneous measurement of velocity and temperature field (Misyura *et al.* 2019; Volkov & Strizhak 2021; Voulgaropoulos *et al.* 2022). Voulgaropoulos *et al.* (2022) combined 2c-PLIF, μPIV and IR thermometry to study bubble dynamics and heat transfer in pool boiling. They achieved the simultaneous measurement of velocity and temperature fields near the bubble, as well as the temperature field of the substrate, providing detailed fluid flow and heat transfer information in bubble lifecycles. Their work demonstrated the feasibility of simultaneously acquiring velocity and temperature fields outside the phase interface (bubble), which could help to quantify the essential aspects of convection heat transfer during the pool boiling bubble growth and departure process. However, the simultaneous measurement of multiple physical fields within dynamic droplet interfaces remains a challenge to be addressed.

In this paper, we utilized 2c-PLIF and μPIV technologies to obtain quantitative velocity and temperature fields of the droplet impingement process with high temporal and spatial resolution. We introduced an image distortion correction method based on astigmatism theory that is applicable to objects with dynamic interfaces. Using this method, we studied water droplet impingement onto a heated wall with different temperatures. We discovered the hot spots at the solid–liquid interface for the first time. Furthermore, the internal flow and heat transfer mechanisms were discussed within different droplet boiling regimes.

2. Experimental methods

2.1. *Experimental system*

The experimental method was based on the simultaneous use of 2c-PLIF and μPIV principles. Schematics of the experimental system for both side view and bottom view imaging are shown in figures 1(*a*,*b*). To minimize the influence of environments on the droplet impingement process, experiments were conducted within a sealed aluminum alloy test chamber. The temperature, humidity and pressure of the surrounding environment

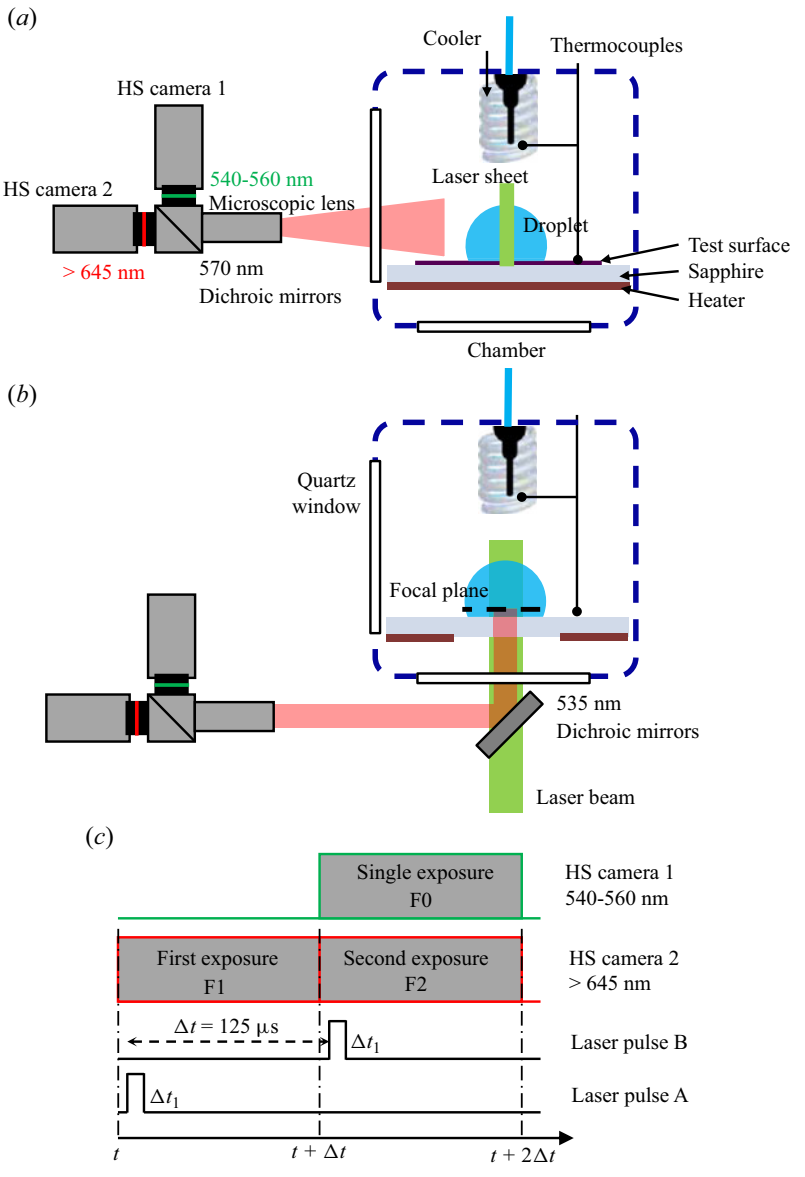

Figure 1. Schematic of the experimental system. (*a*) Side view imaging. (*b*) Bottom view imaging. (*c*) Timing of camera exposures and laser pulses in minimum period.

were controlled. The chamber measured 30 cm × 15 cm × 15 cm, and each side was opened with quartz observation windows to allow for high-speed (HS) camera recording and laser exposure. The chamber was equipped with a three-dimensional displacement platform, allowing for precise position adjustment. The heated surface comprised a polished silicon experimental substrate, a sapphire base (50 mm diameter, 5 mm thickness), an annular ceramic heating plate, and a heat insulation board. The ceramic heater was connected with an external direct current source. The temperature of the experimental substrate was measured with a T-type thermocouple. The sapphire base and the silicon substrate exhibited good heat conduction properties, and IR measurements

(figure 19 in the Appendix) showed a temperature fluctuation less than 1 °C when the silicon substrate was heated up to 282 °C, indicating uniform heating across the entire surface from the sapphire base to the experimental substrate.

A two-pulse μPIV laser was used to generate a two-pulse laser of 527 nm with frequency 4 kHz for each laser pulse. The time interval between two laser pulses was $\Delta t = 125$ μs. For side view imaging, the laser was then converted into a vertical laser sheet using a cylindrical concave lens ($f = -200$ mm) incident into the droplet through the droplet centre from the side direction. For bottom view imaging, the droplet was illuminated with a laser beam through the transparent quartz window. As calculated, the thickness of the laser sheet was less than 0.2 mm at its thinnest position. Fluorescence dyes within the droplet were excited by the 527 nm laser at the same time, and emitted fluorescence signals of different wavelengths. Three types of fluorescent dye were seeded into the fluid (which will be detailed in § 2.2), and the fluorescence signals were captured by an HS microscopic photography system including two HS cameras, a long-distance microscopic lens, a 570 nm dichroic mirror, a 540–560 nm band-pass filter and a 645 nm long-pass filter. For bottom view imaging, an additional 45 ° tilted 535 nm dichroic mirror was placed under the sapphire substrate and the quartz window. The illuminating light source of the 527 nm laser beam can be transmitted, and fluorescence signals with wavelength >540 nm are reflected to the two HS cameras. The clear aperture of the microscopic lens was 63 mm, with numerical aperture 0.08–0.14. The depth of field could be calculated with the Rayleigh criterion, resulting in less than 55 μm for fluorescence signals of wavelength <700 nm. The two cameras were spatially calibrated using a calibration plate to the same field of view region. The spatial resolution after calibration was 3.259 μm.

The laser and cameras were synchronized using a programmable timing unit. The laser pulse and camera exposure time in each minimum period were set as shown in figure 1(*b*). The HS camera 1 was exposed only in the second half to capture the fluorescence signal excited by laser pulse B, while HS camera 2 was exposed twice, with time interval 125 μs. The three frames were named F0, F1 and F2 – F0 and F2 were used to calculate the temperature field, while F1 and F2 were used to calculate the velocity field.

2.2. *Measurement principles*

The velocity measurement was based on the μPIV method. The selection of μPIV tracing particles needs to be considered from two perspectives. First, the particle diameter should strike a balance between being able to be photographed clearly and providing higher spatial resolution. The distribution of particles should not be too dense or too sparse. Second, the tracer particles must be able to accurately follow the flow field and avoid relative slippage as much as possible. In our experiments, μPIV tracing fluorescence particles of 1 wt% were added into the fluid, with diameter $d_p = 2$ μm and density $\rho_p = 1.05 \times 10^3$ kg m^{-3}. The particle distribution was ∼70 particles in a 0.5 mm × 0.5 mm window of images. The identities of particle and flow motion can be evaluated by the particle Stokes number $St_p = \tau_p/\tau_f$ (Raffel *et al.* 2018). Among them, $\tau_p = d_p^2(\rho_p - \rho_l)/18\mu_l$ (where ρ_l and μ_l are the density and dynamic viscosity of the fluid) represents the relaxation time scale of the particle, and $\tau_f = D_0/U_0$ (where D_0 is the initial diameter of the droplet, and U_0 is the impingement velocity). The physical properties of the fluid can be found in table 1. In our experiments, $St_p \sim 10^{-5} \ll 1$, indicating that the tracing particles were able to track the flow field accurately.

Parameter	Symbol	Value	Unit
Density (water, 20 °C)	ρ_l	998	kg m^{-3}
Dynamic viscosity (water, 20 °C)	μ_l	9.54×10^{-4}	Pa s
Surface tension (water, 20 °C)	σ	0.0724	N m^{-1}
Specific heat (water, 20 °C)	$C_{p,l}$	4183.4	J kg^{-1} K^{-1}
Thermal conductivity (water, 20 °C)	λ_l	0.6	W m^{-1} K^{-1}
Droplet diameter	D_0	2.39 ± 0.09	mm
Impingement velocity	U_0	0.4 ± 0.01	m s^{-1}
Droplet initial temperature	$T_{d,0}$	22 ± 3	°C
Weber number	$We = \rho_l U_0^2 D_0/\sigma$	5.3	

Table 1. Physical properties of the fluid and parameters of the droplet.

Temperature measurement was based on the 2c-PLIF method, combined with μPIV to allow us to obtain simultaneous distribution of both velocity and temperature. The LIF technique is flow visualization based on the variation of excited fluorescence signal intensity with temperature, concentration and pH. In a micro-volume dV, the signal intensity F is (Chaze *et al.* 2016)

$$F = \chi \frac{\Omega}{4\pi} \varepsilon_0 \phi \frac{I_0}{1 + I_0/I_{sat}} C \, \mathrm{d}V, \tag{2.1}$$

where χ is the transmission efficiency of the signal to the camera, Ω is the solid angle of the region, C is the molar concentration of the fluorescent dye, ϕ is the fluorescence quantum yield, I_0 is the incidence laser intensity, ε_0 is the molar extinction coefficient, and I_{sat} is the saturation intensity of the fluorescent dye. In this paper, we used a laser sheet to confine the observation region to the droplet symmetry plane, and used two LIF dyes to improve measurement accuracy, thus the method is called 2c-PLIF. The two types of fluorescent dyes, namely Fluorescein sodium (FL, 7×10^{-5} mol l^{-1}) and Sulforhodamine 101 (SR, 1.4×10^{-6} mol l^{-1}), were added into the fluid. With the dichroic mirror and filters, the FL signal was captured mainly by HS camera 1, and SR and μPIV tracing signals were captured mainly by HS camera 2. The SR dye is temperature-insensitive, and the FL dye is temperature-sensitive; the ratio $R(T)$ of the two fluorescence intensities is

$$R(T) = \frac{F_{FL}(T)}{F_{SR}(T)} \propto \frac{\varepsilon_{0,FL}(T)}{\varepsilon_{0,SR}(T_0)} \frac{\phi_{FL}(T)}{\phi_{SR}(T_0)} \frac{C_{FL}}{C_{SR}} \frac{1 + \dfrac{I_0}{I_{sat,SR}}}{1 + \dfrac{I_0}{I_{sat,FL}}}. \tag{2.2}$$

Using the ratiometry method, the fluorescence signal change due to laser non-uniformity and concentration variation was corrected (Chaze *et al.* 2017; Castanet *et al.* 2018, 2020; Voulgaropoulos *et al.* 2022), and ratio $R(T)$ is a function of T. This method is necessary, especially for droplet impingement measurement where dynamic interface and evaporation can lead to laser non-uniformity and concentration variation. With proper temperature calibration, the temperature field could be measured. Because SR signal intensity will decay at a temperature above 60 °C (Chaze *et al.* 2017), we used a flow through a 2 mm thick cuvette to calibrate the temperature in the range 15 °C–99 °C. As shown in figure 2,

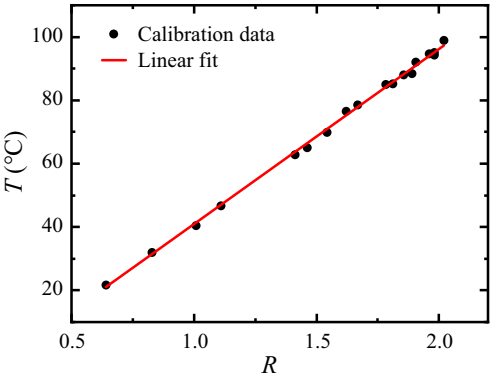

Figure 2. Temperature calibration curve of temperature T as a function of fluorescence intensities ratio R.

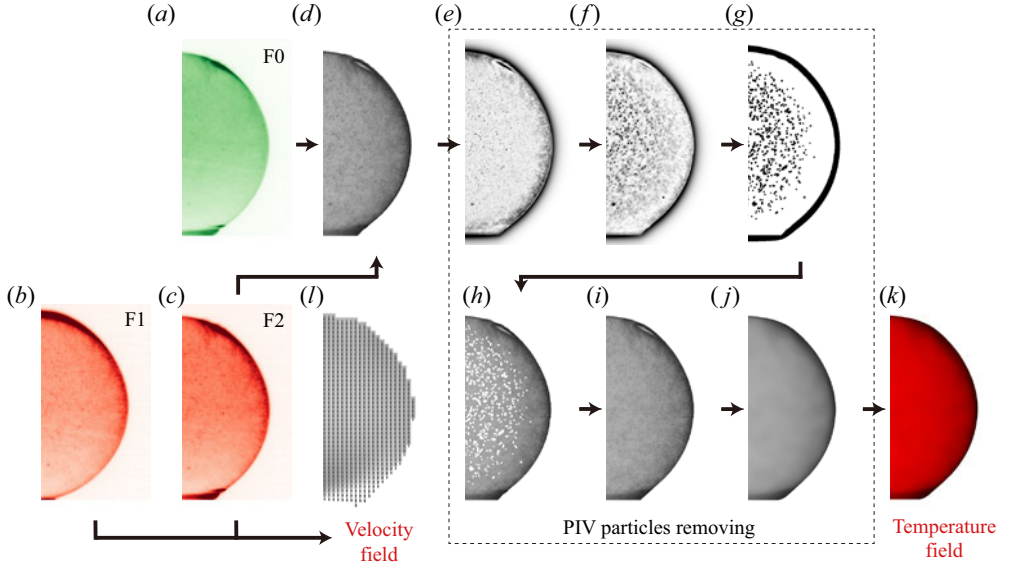

Figure 3. Post-processing procedures: (*a*) raw fluorescence image F0; (*b*) raw fluorescence image F1; (*c*) raw fluorescence image F2; (*d*) F0/F2; (*e*) after subtracting sliding average; (*f*) after inverting and dilation filter; (*g*) after binarization; (*h*) after removing μPIV tracing particle regions; (*i*) after linear interpolation in MATLAB; (*j*) after median filter; (*k*) temperature field; (*l*) velocity field.

the calibration result was fitted to a linear fitting curve:

$$T = 55.53\,R(T) - 14.86\ (^{\circ}\mathrm{C}), \tag{2.3}$$

where $R(T)$ is the processed ratio between FL and SR signal intensities. The velocity field measurement was based on μPIV using the acquired frames F1 and F2, which will be described in § 2.3.

2.3. *Post-processing methods*

The raw images recorded needed to be post-processed to acquire the final temperature and velocity field. The HS camera 2 contained both SR and μPIV tracing particle signals, which needed separation. The post-processing procedure is shown in figure 3. Figures 3(*a–c*) represent the raw frames F0–F2. The first step was to correct the fields

of view of two cameras to the same region using a pre-acquired spatial calibration relationship. Figure 3(*d*) is the ratio s of spatially corrected F0 and F2, in which the influence of μPIV tracing particles on ratio s is significant. The image then subtracted the sliding average of 15 × 15 pixels to find the particles, as shown in figure 3(*e*). It was then processed with a dilation filter of 5 × 5 pixels to enlarge the particle region, binarized, and multiplied by figure 3(*d*) to remove the particle regions, as shown in figures 3(*f–h*). The blank pixels were then linearly interpolated, as shown in figure 3(*i*). The influence of μPIV tracing particles on temperature measurement is greatly reduced by the above steps. The image in figure 3(*i*) was then smoothed using a 43 × 43 median filter, as shown in figure 3(*j*). As shown in figure 3(*k*), it was converted to a temperature field using the temperature calibration curve and initial droplet temperature

$$T = f\left(\frac{s}{s_0} f^{-1}(T_0)\right), \tag{2.4}$$

where T_0 denotes the initial temperature, and s_0 denotes the average signal before the droplet contacts the substrate. As shown in figure 3(*l*), The velocity field was calculated using images F1 and F2. The initial search window was 256 × 256 pixels with 50 % overlap, and the second search windows were four times 64 × 64 pixels with 75 % overlap. The resolution of the velocity field was 52.14 μm.

The ratiometric method can eliminate the effects of laser non-uniformity raised from the reflection and refraction of the laser sheet through the liquid–gas interface (Chaze *et al.* 2017; Castanet *et al.* 2020). The uncertainty of the 2c-PLIF method σ_T consists mainly of the signal noise of HS cameras σ_s and the calibration error σ_c. Chaze *et al.* (2016) provided an approach to evaluate $\sigma_s = (RMS/R)/s$, where RMS represents the root mean square of the fluorescence intensities ratio image F_{FL}/F_{SR}, R represents the averaged fluorescence ratio from the image, and s represents the sensitivity of the fluorescence ratio to temperature. The sensitivity s is defined by Chaze *et al.* (2016) as

$$s = \frac{\ln(R(T_1)/R(T_2))}{T_1 - T_2} \times 100\,\%, \tag{2.5}$$

where $R(T_1)$ and $R(T_2)$ are the fluorescence ratios at the highest and lowest temperatures (T_1 and T_2, respectively) in the calibration curve. The sensitivity is calculated as 1.498 % per °C. Also, the calibration error is defined as $\sigma_c = |T - T_c|$, where T represents the temperature calculated with the calibration curve at the fluorescence ratio R, and T_c represents the temperature measured during the calibrating process. As σ_s originates from the random noise of HS cameras, the two sources of uncertainties can be regarded as mutually independent. The overall uncertainty can be calculated with the propagation law of error $\sigma_T = \sqrt{\sigma_s^2 + \sigma_c^2}$. Figure 4(*d*) shows the overall uncertainty for each calibration point. Hence the uncertainty of temperature measurement is expected to be ±1.7 °C. The substrate temperature was measured using a K-type thermocouple with uncertainty ±0.8 °C.

The uncertainties of μPIV measurements are quantified using the method of Sciacchitano *et al.* (2015). The error distributions of the velocity magnitude, and velocity components in the x and y directions, are shown in figures 5(*b–d*). The relative velocity error $U_{err}/|U|$ and relative error of each velocity component can be calculated, with over 72 % of velocity vectors having relative uncertainty <10 %, and over 87 % of velocity vectors having relative uncertainty <20 %. The vectors having relative uncertainty greater than 20 % mainly have a small velocity magnitude, which makes μPIV calculations harder and raises the uncertainty.

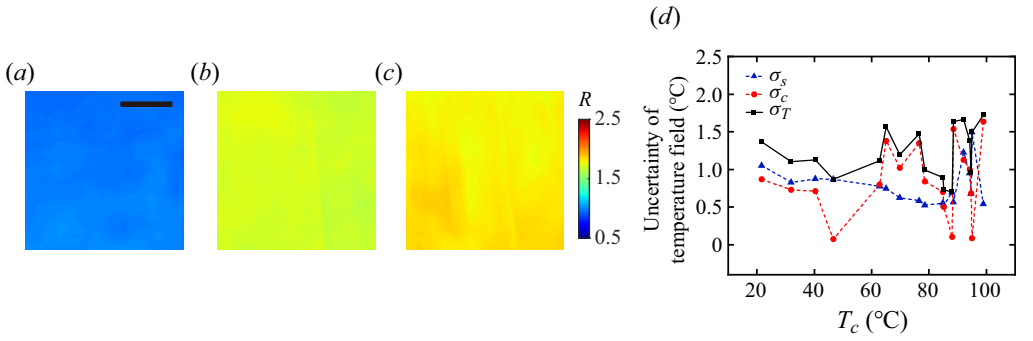

Figure 4. Fluorescence ratio images of (*a*) $T_c = 44.0\,^{\circ}\mathrm{C}$, (*b*) $T_c = 78.6\,^{\circ}\mathrm{C}$, (*c*) $T_c = 99.0\,^{\circ}\mathrm{C}$. The black bar represents a length scale of 0.5 mm. The colour bar shows the values of fluorescence intensities ratio R. (*d*) The signal noise σ_s, calibration error σ_c and overall uncertainty σ_T for each calibration temperature.

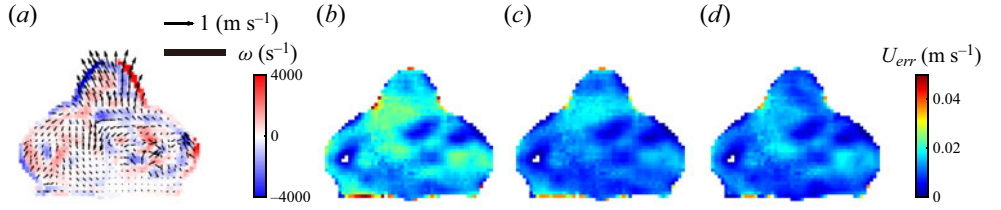

Figure 5. (*a*) Detailed velocity field and vorticity field for $T_w = 359\,^{\circ}\mathrm{C}$, $t = 6$ ms. (*b–d*) Uncertainty calculated with the method of Sciacchitano *et al.* (2015): (*b*) velocity magnitude uncertainty U_{err}; (*c*) uncertainty of velocity in the x direction, u_{err}; (*d*) uncertainty of velocity in the y direction, v_{err}. The black bar represents a length scale of 1 mm, and the arrow represents velocity scale of 1 m s^{-1}. The colour bar in (*a*) shows the value of vorticity ω. The colour bar in (*b–d*) shows the value of velocity magnitude uncertainty U_{err}.

Another error of droplet internal flow visualization arises from the image distortion due to refraction at the droplet dynamic interface (Kang *et al.* 2004; Chaze *et al.* 2017; Bouillant *et al.* 2018). We introduced image distortion analysis by reconstructing the refraction light path across the droplet interface. We first recognize the droplet outline in each frame, rotate the outline by one complete revolution around the axis of symmetry (passing through the droplet centre of mass, along the height axis), and then obtain the reconstructed droplet three-dimensional interface. The images captured by cameras are regarded to be located on the central plane of the droplet; the actual luminous point will have a shift on the central plane after the refraction at the droplet interface. With our image distortion correction method, this shift could be calculated. A sample result is shown in figure 6, where figure 6(*a*) is a raw image, and figure 6(*b*) is the corresponding 'real' image after correction.

2.4. *Experimental cases*

A droplet with diameter D_0 was generated using a needle and a micro-syringe pump. As the highest temperature of the substrate was $\sim 360\,^{\circ}\mathrm{C}$ during experiments, fluid in needle could be heated up. To eliminate this effect, the needle was cooled by water-cooled coils to control the droplet's initial temperature to $T_{d,0}$. Droplets fell onto a heated smooth silicon

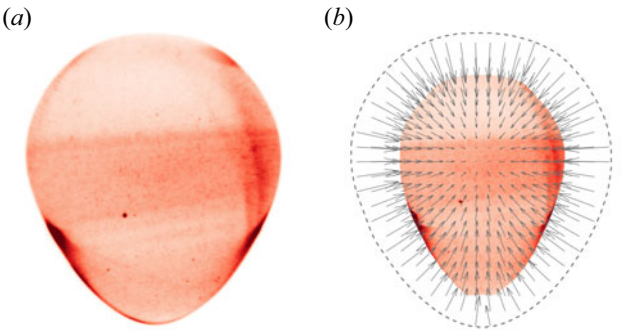

Figure 6. (*a*) Raw fluorescence image. (*b*) Image after image correction. The grey dashed line represents the original droplet boundary, and the grey vectors represent the position shift from the raw image to the corrected image.

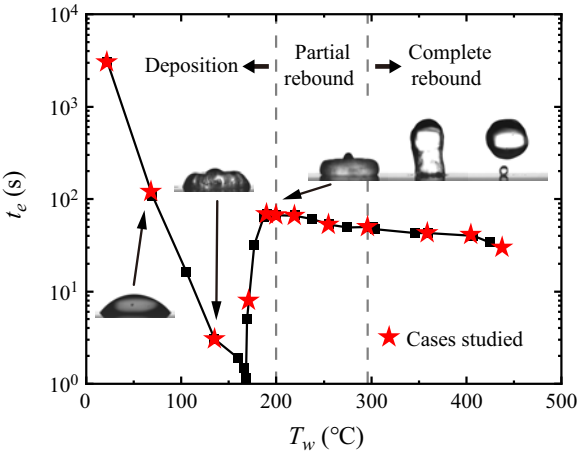

Figure 7. Droplet evaporation time at different wall temperatures, where typical morphological phenomena at different wall temperatures are shown. The red stars represent cases studied with the use of the experimental system mentioned before. The grey dashed lines mark the transition wall temperatures $T_w = 200\,^{\circ}\mathrm{C}$ and $296\,^{\circ}\mathrm{C}$ of different droplet impingement outcomes: deposition, partial rebound and complete rebound.

substrate with impingement velocity U_0. The silicon substrate's contact angle at room temperature was 60°. Parameters of impinging droplets are shown in table 1.

According to the droplet evaporation time curve (figure 7) and droplet morphologies (see figure 9 below), we can separate the boiling regimes into evaporation, nucleate boiling and contact boiling regimes (within the wall temperature range in our experiments). When the wall temperature T_w was increased from 22 °C to 100 °C, the droplet evaporation time decreased from 50 min to ∼10 s. At this point, the wall temperature did not reach the saturation temperature, and droplets experienced only evaporation after impingement. From 100 °C to 171 °C, the boiling regime changed to nucleate boiling, causing the fluid to contact the substrate and generate bubbles. When $T_w > 171\,^{\circ}\mathrm{C}$, the droplets entered the contact boiling regime. The droplets experienced contact boiling first, then formed a vapour film under a portion of the contact area between droplets and substrate, resulting in an increase in the evaporation time. Above 200 °C, the evaporation time slowly decreased. Droplets rebounded after the first impact, instead of being deposited on the

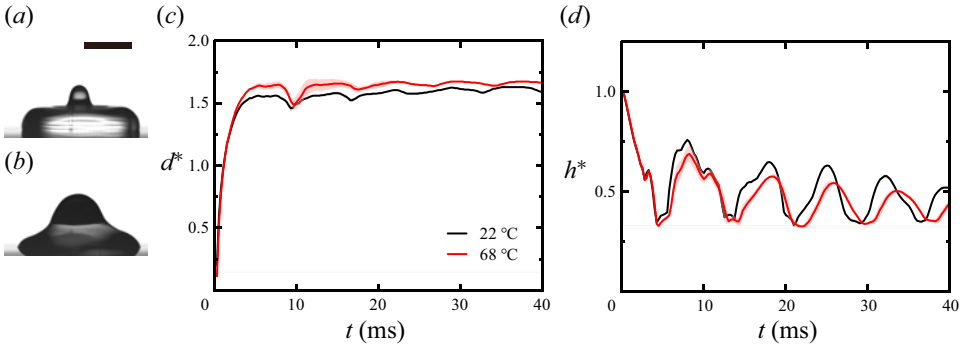

Figure 8. Droplet impingement in the evaporation regime: (*a*) spreading stage, $T_w = 68\,^{\circ}\mathrm{C}$, $t = 4.5$ ms; (*b*) recoiling stage, $T_w = 68\,^{\circ}\mathrm{C}$, $t = 7.75$ ms. The black bar represents a length scale of 1 mm. (*c*) Dimensionless droplet spreading diameter. (*d*) Dimensionless droplet centre height when $T_w < 100\,^{\circ}\mathrm{C}$. The error band represents the standard deviation of three repeated experiments.

substrate for T_w less than 200 °C. Droplet rebounding morphologies can be categorized into partial rebound ($T_w < 296\,^{\circ}\mathrm{C}$) and complete rebound ($T_w > 296\,^{\circ}\mathrm{C}$), as shown in supplementary material figures S1 and S2 (available at https://doi.org/10.1017/jfm.2024.751). The transitions of droplet dynamics from deposition to partial or complete rebound are marked in figure 7. As shown in figure 7, we selected several wall temperatures (in °C) to study the corresponding internal temperatures and velocity fields during droplet impingement in the 20 ms after impingement: 22, 68, 135, 171, 190, 200, 219, 255, 296, 359.

3. Results and discussions

3.1. *Droplet morphology*

In the first 20 ms after impingement, all the studied droplets experienced the process of 'spread–recoil'. The differences caused by different surface temperatures include mainly that the main phenomenon of the phase transition of the droplets is different, the dynamic spreading and retracting processes of the droplets are not synchronized, and whether the droplets finally detach from the surface. As shown in figures 8(*a*,*b*) and supplementary material figures S1 and S2, when $T_w < 100\,^{\circ}\mathrm{C}$, no boiling behaviour or bubble formations were observed in the spreading stage or the recoiling stage. After the droplet stopped recoiling, the surface wave started to propagate, and the droplet turned into an oscillating stage. With higher wall temperature, the droplet could be heated to a higher temperature and thus a lower surface tension σ. Lamb (1924) and Cummings & Blackburn (1991) showed that the propagation speed of the surface wave was $\propto \sigma^{1/2}$, and the oscillation period was $\propto \sigma^{-1/2}$, which indicated that droplets impinging onto surfaces with higher T_w have smaller surface wave propagation speed. Furthermore, when the impinging droplet reaches maximum spreading, a lower surface tension can lead to a larger spreading radius, as the interface energy transforming from kinetic energy is directly proportional to σ. This could result in a larger spreading radius, a longer recoiling time, and a longer oscillation period, which are shown in the time variations of spreading radius and centre height in figures 8(*c*,*d*).

When T_w was 135–190 °C, nucleate boiling was observed, and the droplets did not rebound during the first impingement. As shown in figures 9(*a*,*b*), many boiling bubbles

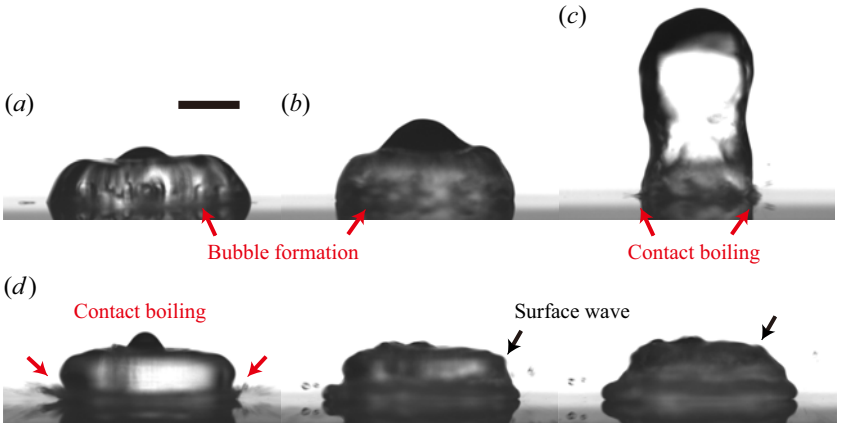

Figure 9. Boiling phenomena at different T_w: (*a*) bubble formation, $T_w = 135\,^{\circ}\mathrm{C}$, $t = 3.25$ ms; (*b*) bubble formation, $T_w = 171\,^{\circ}\mathrm{C}$, $t = 6$ ms; (*c*) contact boiling, $T_w = 190\,^{\circ}\mathrm{C}$, $t = 10.5$ ms; (*d*) contact boiling and surface wave propagation, $T_w = 215\,^{\circ}\mathrm{C}$, $t = 3.25$–3.75 ms. The black bar represents a length scale of 1 mm.

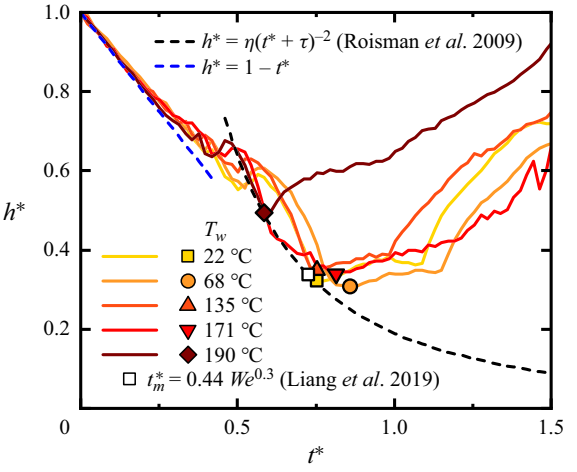

Figure 10. Dimensionless droplet centre height when $22\,^{\circ}\mathrm{C} \leq T_w \leq 190\,^{\circ}\mathrm{C}$; symbols of scatter plots represent droplets reaching minimum height. The black dashed line gives the dimensionless centre height model $h^* = \eta(t^* + \tau)^{-2}$ (Roisman *et al.* 2009), with $\eta = 0.23$, $\tau = 0.1$. The white square represents a maximum spreading time of a droplet impacting on a room temperature surface from model $t_m^* = 0.44\,We^{0.3}$ (Liang *et al.* 2019).

were formed at the droplet–wall interface, but their growth was slow and did not merge or cause droplet splashing. When $T_w = 171\,^{\circ}\mathrm{C}$, the bubble formation and the liquid–gas surface oscillation were more violent. This temperature is close to the minimum evaporation time of droplets (168 °C). When $T_w = 190\,^{\circ}\mathrm{C}$, the contact boiling and the induced splashing could be observed (figure 9*c*).

Figure 10 shows time evolution of dimensionless centre height h^* for droplets in evaporation and nucleate boiling regimes. In the very early stage of impact (the so-called kinetic phase), the reaction force from the substrate hardly affect the top of the droplet. The height of droplets declines with speed U_0, so in this stage, centre height can be represented as a simple expression $h^* = 1 - t^*$. The time of the kinetic phase was limited to $t^* < 0.1$. After droplets start to spread out and reach the spreading phase, the wall effect has to be considered. Roisman *et al.* (2009) gave an expression $h^* = \eta(t^* + \tau)^{-2}$ based

on the inviscid remote asymptotic solution (Yarin & Weiss 1995). In our experiments of evaporating and boiling droplets, we also found a good fit with $h^* = 0.23(t^* + 0.1)^{-2}$ in the spreading stage of $t^* < 0.6$. After turning into the recoiling regime, effects of boiling bubbles started to dominate. Frequent contact boiling provided pressure pointing to the inside of the droplet, produced frequent surface waves, and forced the droplet to recoil with a hydrophobic contact angle. As a result, the boiling droplets' centre rose earlier, and the minimum centre height was larger than droplets in evaporation regimes.

When T_w was 200 °C–255 °C, boiling caused massive random oscillation at the droplet interface, and all the droplets rebounded after the first impingement. Compared with $T_w =$ 190 °C, when $T_w = 215$ °C, as shown in figure 9(*d*), the contact boiling and the satellite droplets' atomization was more violent. The generated surface wave propagated upwards, providing momentum for the droplet rebounding. As the wall temperature is increased further ($T_w = 296$ °C–359 °C), the surface oscillation starts reducing due to the formation of a vapour layer. Beyond our studied wall temperature range, if the wall temperature is greater than the Leidenfrost temperature T_L, then the vapour layer beneath the droplet would be completely formed and the dynamic Leidenfrost effect could be observed (Tran *et al.* 2012; Shirota *et al.* 2016).

The above analysis on droplet morphology indicates that wall heating's influences on droplet morphology are increasing droplet spreading and oscillation for evaporating droplets, and inducing boiling that caused droplets to rebound for boiling droplets.

3.2. *Influence of internal mixing of droplets on the contact time*

The measurements of droplets' internal velocity fields could help us to quantify the influence of wall temperature on droplets' internal flow and mixing characteristics. The internal velocity and vorticity fields are shown in figure 11 and supplementary material figure S3. Vorticity is defined as $\omega = \partial v/\partial x - \partial u/\partial y$. For T_w above 100 °C, bubbles generated from violent nucleate boiling rapidly grow and rise up, inducing intensive mixing inside the droplet. The absolute value of velocity and non-uniformity greatly increased, especially for wall temperatures 190 °C–200 °C.

After reaching the contact boiling regime and increasing the wall temperature above 200 °C, the violent contact boiling could generate a surface wave and facilitate the rebound of droplets (instead of sticking on the substrate). The velocity distribution shown in figure 11 indicates a massive mixing inside a contact boiling droplet. For dynamic Leidenfrost droplets, the internal flow is driven by the recoiling of the droplet surface with a small scale of mixing. Schematic diagrams for droplet morphological phenomena and internal flow patterns of contact boiling and dynamic Leidenfrost droplets are given in figures 12(*a*,*b*). It is well known that the vapour layer shown in figure 12(*b*) makes droplets highly mobile (Graeber *et al.* 2021; Yang *et al.* 2023). In contrast, during the contact boiling regime, a partially covered vapour layer is formed (Shirota *et al.* 2016; Castanet *et al.* 2020), as illustrated in figure 12(*a*). The droplets maintain contact boiling with the heated substrate, introducing additional internal mixing and dissipation that hinder droplet recoil and rebound. The underlying competition relationship between the vapour layer and the contact boiling requires further quantified descriptions.

Figure 12(*c*) indicates a uniform time scale $t_{max} \approx 3.5$ ms for rebounding droplets to reach their maximum spreading; however, the time for droplets to recoil and bounce off the substrate shows a difference with different wall temperature. Typical Leidenfrost droplets' contact time is dominated by inertia and capillarity, which can be expressed as

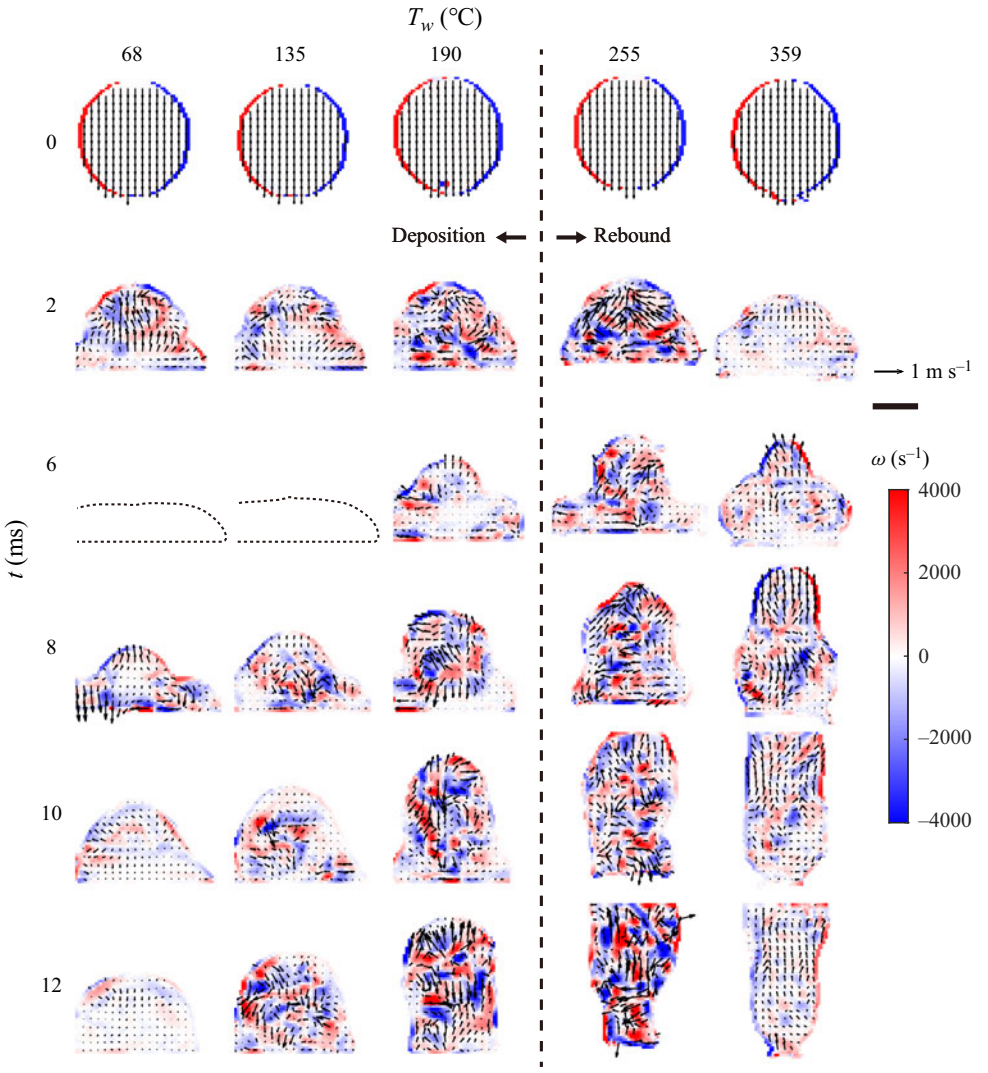

Figure 11. Internal velocity and vorticity fields at different wall temperatures in the 12 ms after impingement. The colour bar shows the value of vorticity ω; the vectors indicate the magnitude and direction of velocity field. A unit vector of 1 m s^{-1} is given. The black bar represents a length scale of 1 mm. Measurement results of droplets with a compressed shape in the spreading stage are not used for analysis.

the inertia–capillary limit (Richard, Clanet & Quéré 2002; Huang, Lo & Lu 2022)

$$t_\sigma = \frac{\pi}{4}\sqrt{\frac{\rho D_0^3}{\sigma}}. \tag{3.1}$$

The density ρ and the dynamic viscosity μ are calculated as temperature-dependent physical properties at the average temperature within the time period from impact to rebound of the droplet. Increasing wall temperature led to a decrease in droplet–wall contact time t_c to the theoretical inertia–capillary limit, which suggests that boiling bubbles and violent internal mixing can increase the internal dissipation, reduce the mean upward velocity, and result in a slower rebound, as illustrated in figure 12(*d*). Previous

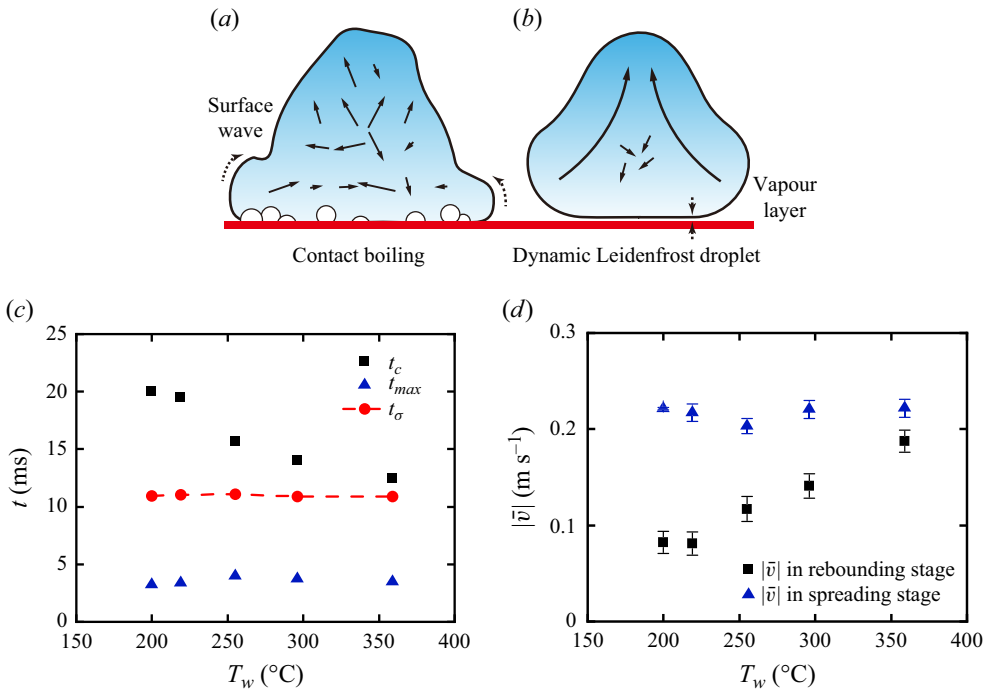

Figure 12. Schematic diagrams for (*a*) a contact boiling droplet and (*b*) a dynamic Leidenfrost droplet. (*c*) Relationship between droplet–wall contact time t_c, spreading time t_{max} and wall temperature. Red circles with dashed line represent the inertia–capillary limit t_σ. (*d*) Average absolute velocity in the y direction, $|\bar{v}|$, calculated from velocity fields. The error is estimated with the method described in § 2.3.

studies have already proved that viscous dissipation could have a significant influence on the droplet spreading and bouncing dynamics (Wildeman *et al.* 2016; Sanjay, Chantelot & Lohse 2023). To further verify our expectations, we can calculate the local viscous dissipation rate with the direct measurement of velocity distribution:

$$\phi = \mu \left[2\left(\frac{\partial u}{\partial x}\right)^2 + 2\left(\frac{\partial v}{\partial y}\right)^2 + \left(\frac{\partial u}{\partial y} + \frac{\partial v}{\partial x}\right)^2 \right]. \tag{3.2}$$

Integrating the viscous dissipation rate with element time and volume, we can calculate the overall energy dissipation:

$$E_\mu = \int_0^t \int_{V_d} \phi \, \mathrm{d}V \, \mathrm{d}\tau. \tag{3.3}$$

Figure 13(*a*) gives the dimensionless energy dissipation $E_\mu/E_{k,0}$ in the recoiling stage as a function of dimensionless time t^*. Here, $E_{k,0} = (\pi/12)\rho_l D_0^3 U_0^2$ represents the initial kinetic energy of a droplet. The dissipation rate increases slightly with time. Then we calculate the average dimensionless dissipation rate for each rebounding droplet with different wall temperatures:

$$\bar{\phi}^* = \frac{\phi}{\phi_0}, \quad \phi_0 = \mu \left(\frac{U_0}{D_0}\right)^2, \tag{3.4a,b}$$

where ϕ_0 represents the characteristic scale of dissipation rate. Figure 13(*b*) shows the relationship between $\bar{\phi}^*$ and wall temperature T_w, which is consistent with the trend of

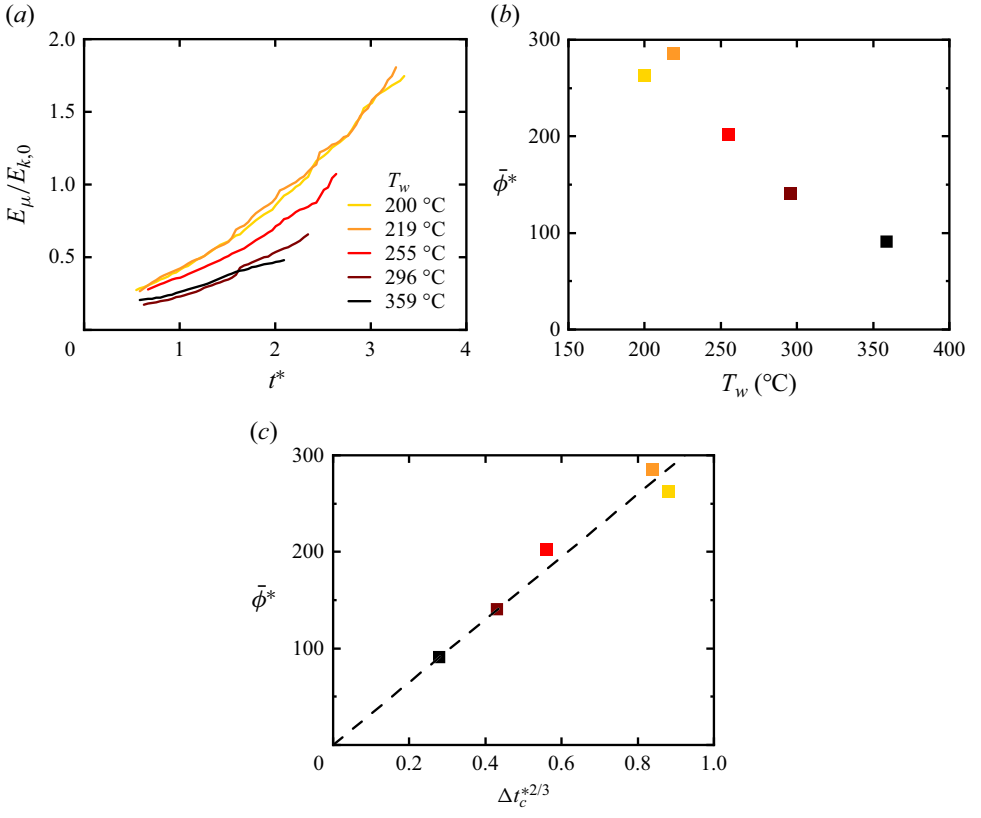

Figure 13. Analysis of the internal viscous dissipation. (*a*) Dimensionless overall energy dissipation E_μ as a function of dimensionless time t^*. (*b*) Relationship between average dimensionless dissipation rate $\bar{\phi}^*$ and wall temperature T_w. (*c*) The correlation between $\bar{\phi}^*$ and dimensionless contact time increment Δt_c^*. The best fitting can be expressed as $\bar{\phi}^* = 325\Delta t_c^{*2/3}$ (black dashed line).

the declining contact time. To demonstrate the additional effect of wall temperature and the internal mixing induced by boiling, we calculate the increments of contact time with the inertia–capillary limit as $\Delta t_c = t_c - t_\sigma$. As shown in figure 13(*c*), the dimensionless dissipation rate shows a good scaling correction $\bar{\phi}^* \propto \Delta t_c^{*2/3}$, where $\Delta t_c^* = \Delta t_c/t_\sigma$ is the dimensionless contact time increment.

3.3. *Droplet heat transfer characteristics at different wall temperatures*

Different wall temperatures will not only affect the droplets' morphological changes and internal velocity distribution, but also have significant impact on the internal temperature distribution. As mentioned before, boiling phenomena induce the internal mixing, which could influence the heat transfer inside droplets. Direct measurements of internal temperature fields can help us to investigate the influence of wall temperature on microscopic heat transfer processes. The internal temperature fields are shown in figure 14 and supplementary material figure S4.

With increasing wall temperature, the temperature rise was not monotonic, and different temperature rising modes were observed. When $T_w = 68\,^\circ$C, a high temperature layer region was formed near the wall at $t = 2$ ms. Fluid with high temperature was carried to the

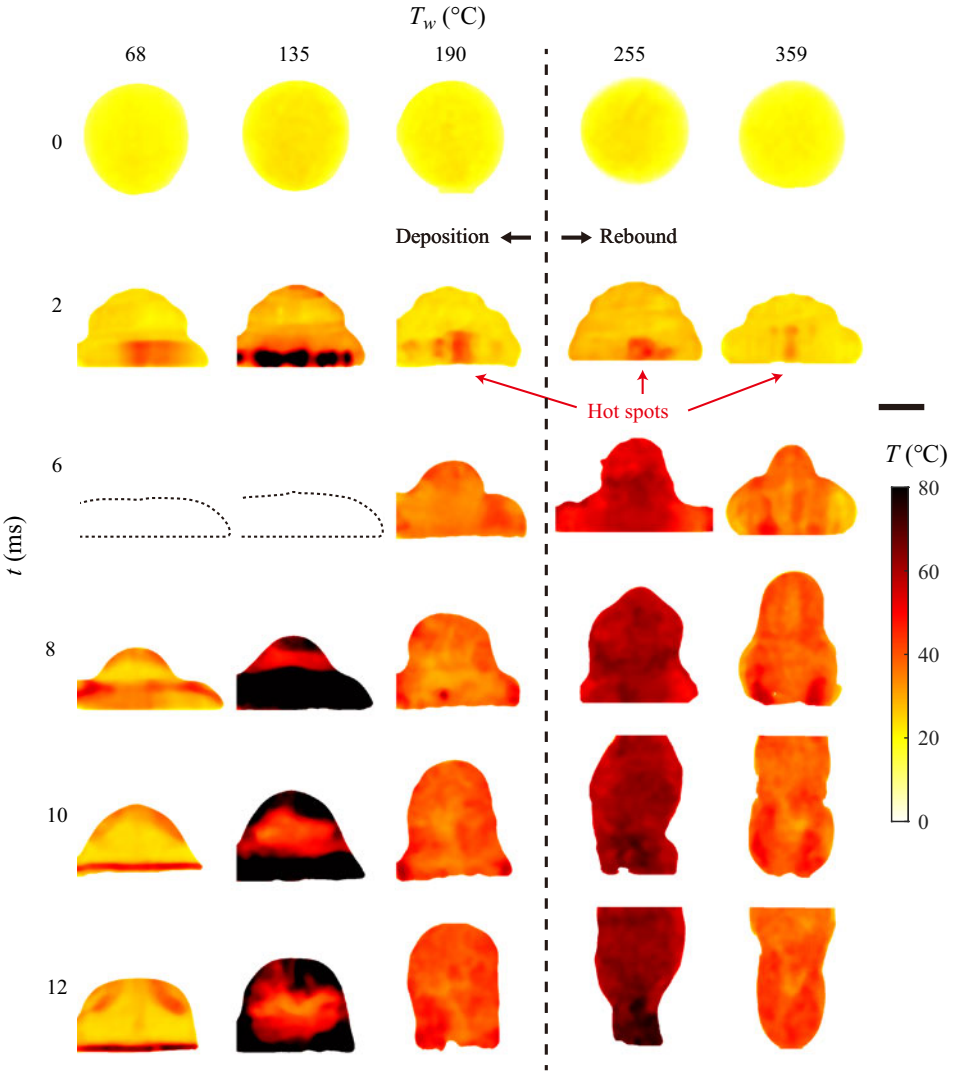

Figure 14. Internal temperature fields at different wall temperatures in the 12 ms after impingement. The colour bar represents the values of internal temperature T. The hot spots at the liquid–solid interface are marked by red arrows. The black bar represents the length scale of 1 mm. Measurement results of droplets with a compressed shape in the spreading stage are not used for analysis.

top of the droplet and mixed together after the droplet recoiled. This internal mixing was the result of both wall heating and droplet oscillating motion. When $T_w = 135\,^{\circ}\mathrm{C}$, a similar internal temperature pattern was observed, but with higher temperature, and the boiling accelerated the internal mixing of fluid with temperature difference. However, when $T_w = 171\,^{\circ}\mathrm{C}$, which is close to the transition point from the nucleate boiling regime to the contact boiling regime (figure 7), the temperature rising was not as high as for a droplet with $T_w = 135\,^{\circ}\mathrm{C}$. This phenomenon indicated that the peak of the average evaporation rate occurs at a higher wall temperature than the peak of the droplet temperature rise. Boiling near the substrate increases the evaporation rate, creates lots of bubbles, and increases the thermal resistance. Another change in the heat transfer pattern is that the temperature

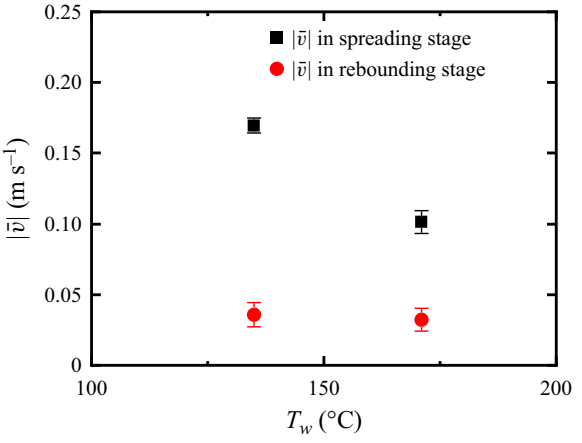

Figure 15. Average absolute velocity in the y direction, $|\bar{v}|$, in the spreading and rebounding stages for $T_w = 135\,^{\circ}\mathrm{C}$ and $171\,^{\circ}\mathrm{C}$.

was more uniform and there was no hot region at the droplet top. Figure 15 shows that the average downward velocity in the spreading stage was lower when $T_w = 171\,^{\circ}\mathrm{C}$. This suggested that the kinetic energy was consumed by more violent internal mixing induced by boiling. The droplet top had a lower downward speed and could not reach the high temperature region near the substrate.

When $T_w = 190\,^{\circ}\mathrm{C}$, the hot region near the wall at 2 ms had a spot-like shape. It is worth mentioning that as shown in figure 14 and supplementary material figure S4, a spot-like region near the wall was observed for $T_w = 190\,^{\circ}\mathrm{C}$–$359\,^{\circ}\mathrm{C}$, indicating that these phenomena existed for contact boiling droplets. Figures 16(*a*,*b*) show the side and bottom views of droplets impinging on a substrate with $T_w = 255\,^{\circ}\mathrm{C}$. Figure 16(*a*) indicates that the hot spot was formed in the very beginning stage at $t = 1.5$ ms, then the high temperature region diffused in both horizontal and vertical directions. The temperature fields acquired from the bottom view in figure 16(*b*) also show that the hot spot starts from the centre of a droplet, then spreads in each direction of the horizontal plane. Temperature profiles in figures 16(*c*,*d*) suggest the spreading of hot spots in the horizontal direction again. The temperature difference between the hottest and coolest points could reach $30\,^{\circ}\mathrm{C}$, which indicates a great non-uniformity in the heat transfer process. After the droplet reached the contact boiling regime, a larger area of vapour film would appear and partially block the heat transfer between droplets and the heated substrate. Droplets preferentially absorbed heat from local areas with small thermal resistance. This non-uniform heat transfer is related to the flow patterns close to the substrate within droplets. After the impact of the cool droplet with the heated substrate, the flow direction changed from the vertical direction to the horizontal direction due to the obstacle effect from the surface, creating a stagnation flow region at the centre of the droplet. These flow patterns can be observed in our velocity measurement results (supplementary material figure S3) and also have been verified by both experimental and numerical results (Wildeman *et al.* 2016; Gultekin *et al.* 2020), which are also similar to the basic flow structure underlying the jet impingement cooling process (Martin 1977; Chen, Xu & Jiang 2021). The stagnation flow region has the highest cooling efficiency on the entire surface, corresponding to the droplet absorbing more heat from the heated substrate at the centre.

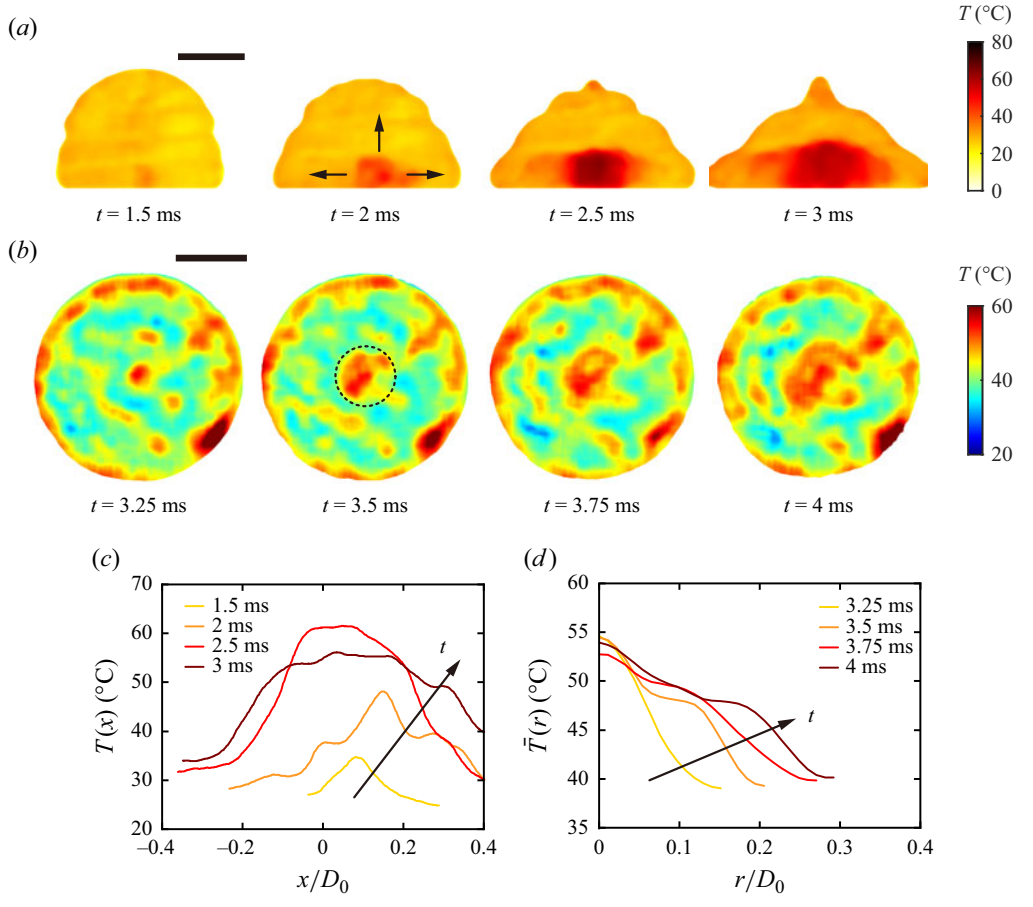

Figure 16. (*a*) Side view and (*b*) bottom view of the internal temperature fields inside droplets impinging on a substrate with $T_w = 255\,^{\circ}\mathrm{C}$. The black bars represent a length scale of 1 mm. The colour bars show the value of internal temperature T. The spot-like region of high temperature is marked with a dashed circle, and the diffusion directions are indicated with arrows. Temperature profiles from (*c*) side view and (*d*) bottom view. The time order of the steps is shown by arrows. The original points of horizontal axis x and radial axis r are settled in the centre points of droplets.

Although the droplet rebounded at $T_w = 200\,^{\circ}\mathrm{C}$ but not $190\,^{\circ}\mathrm{C}$, the droplet temperature fields were very similar, indicating that the rebound mechanism was driven not by the temperature difference liquid, but the more violent contact boiling, as described in § 3.1. When $T_w = 255\,^{\circ}\mathrm{C}$, the droplet temperature rise increased again. As the wall temperature increased to $296\,^{\circ}\mathrm{C}$, the droplet surface vibration was not as violent, and the temperature rise of the droplet was decreased again.

3.4. *The scaling law of a boiling droplet absorbing heat*

With the usage of droplet internal temperature fields, we can calculate the average temperature of droplets $\bar{T}_d$, and evaluate the time evolution of droplet temperature rise with different wall temperature. Furthermore, a scaling law is acquired from the heat transfer model and droplet contact diameter curve. The heat flux at the droplet bottom can be estimated using the one-dimensional heat conduction model (Breitenbach, Roisman &

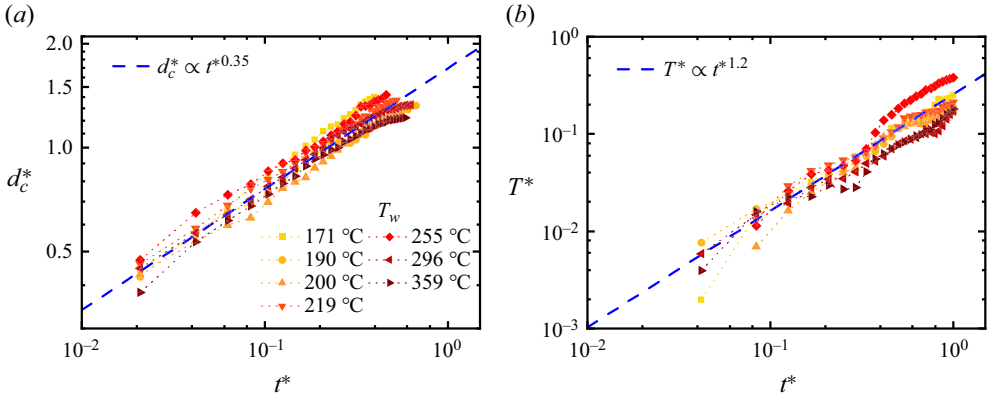

Figure 17. (*a*) Relationship between dimensionless droplet contact diameter d_c^* and t^*. The blue dashed line represents the scaling $d_c^* \propto t^{*0.35}$ for boiling droplets. (*b*) Relationship between dimensionless droplet temperature rise T^* and t^*. The blue dashed line represents the scaling law $T^* \propto t^{*1.2}$.

Tropea 2017; Castanet *et al.* 2018)

$$q_l = \frac{\sqrt{5\rho_l C_{p,l}\lambda_l}\,(T_{lv} - T_{d,0})}{\sqrt{\pi t}}, \tag{3.5}$$

where T_{lv} is the temperature of the droplet bottom interface, which for boiling droplets ($T_w > 100\,^\circ$C) is close to T_{sat} (Liang & Mudawar 2017). The corresponding droplet temperature rise could be calculated using the dynamic contact diameter:

$$\bar{T}_d - T_{d,0} = \frac{1}{mC_{p,l}} \int_0^t q_l(\tau)\,\frac{\pi}{4}\,d_c(\tau)^2\,\mathrm{d}\tau, \tag{3.6}$$

where m is the mass of the droplet. In the kinetic phase ($t^* < 0.1$) of impacting droplets, the dimensionless contact diameter increased with $t^{*0.5}$. However, after reaching the spreading phase, a lamella is ejected, and several parameters, including surface tension, viscosity, droplet diameter and impinging velocity, start to exert an influence (Rioboo, Marengo & Tropea 2002; Castanet, Caballina & Lemoine 2015). Moreover, boiling bubbles and a vapour film formed between the wall and droplets also have a non-negligible effect on the spreading process in boiling regimes. Here, we tracked the contact diameter of droplets with different wall temperatures from morphology photos. As shown in figure 17(*a*), dimensionless droplet contact diameter $d_c^* = d_c/D_0$ increased, with $d_c^* \propto t^{*0.35}$. Then combining with the heat transfer model (3.5) and integral relation (3.6), we can acquire the scaling law of the dimensionless droplet temperature rise:

$$T^* = \frac{\bar{T}_d - T_{d,0}}{T_{sat} - T_{d,0}} = \sqrt{\frac{45}{4\pi}\,\frac{\lambda_l}{\rho_l C_{p,l} D_0 U_0}} \int_0^{t^*} \tau^{*-0.5}\, d_c^*(\tau^*)^2\,\mathrm{d}\tau^* \propto t^{*1.2}. \tag{3.7}$$

Figure 17(*b*) shows good agreement of experimental measurements and scaling law $T^* \propto t^{*1.2}$ for droplets within the contact boiling regime ($T_w \geq 171\,^\circ$C). This scaling law was different in previous work by Liu *et al.* (2022), who provided a $T^* \propto t^{*1.5}$ scaling law within the spreading stage. Both works applied the one-dimensional heat conduction model, and the difference was caused mainly by our employing different droplet spreading

scaling relationships. We used different impact parameters and focused on different droplet boiling regimes (our work considered rebounding droplets within the contact boiling regime; Liu *et al.* (2022) considered sticking droplets, and droplets with splashing and atomization). Thus the different spreading dynamics could be explained.

The droplet impingement heat transfer rate, denoted as Q and defined in (3.8), is used to quantify the heat absorption during the initial impingement of the droplet on the heated substrate:

$$Q = \frac{mC_{p,l}(\bar{T}_d - T_{d,0})}{\Delta t}, \tag{3.8}$$

where $m = \rho_l\,(\pi/6)D_0^3$ represents the mass of a droplet, and Δt represents the time interval. The temperature rise $\bar{T}_d - T_{d,0}$ is calculated within Δt. For deposition droplets, Δt equals a fixed value 20 ms, and for rebounding droplets, Δt equals t_c.

When a droplet reaches the contact boiling regime and deposits on the substrate ($T_w = 171\,^\circ\text{C}$–$200\,^\circ\text{C}$), a vapour layer begins to form, blocking the heat transfer from the substrate to the droplet, and leading to a reduction of Q. When $T_w > 296\,^\circ\text{C}$, the vapour layer almost fully covers the interface between the droplet and the substrate, leaving only a few bubbles inside the droplet caused by contact boiling. The droplet becomes highly mobile and completely rebounds after impingement. The heat transfer rate slightly increases. In this region of wall temperature, the trend of the heat transfer rate curve first decreasing then increasing has already been well studied (Liang & Mudawar 2017) and is consistent with the predicted curve in figure 18.

It is noteworthy that a significant increase in Q is observed for partially rebounding droplets impinging on the substrate with $T_w = 200\,^\circ\text{C}$–$296\,^\circ\text{C}$, which deviates substantially from the predicted curve (figure 18, marked with a red ellipse). As the wall temperature increases, the expanded covered region of the vapour layer enhances the droplet's mobility. The remaining contact boiling region of the droplet exerts a downward force during the rebounding stage, causing the droplet pinch off and resulting in a partial rebound of the droplet. Contact boiling also increases the instability of the partially covered vapour layer, enhancing droplet interface oscillation, and leading to the penetration of the vapour layer. The frequent contacts between the droplet and the heated substrate bring additional heat absorption (figure 9(*e*), supplementary material figures S1 and S2). Our findings indicate that despite the vapour layer's obstruction to overall heat transfer capacity, partially rebounding droplets in the contact boiling regime could still exhibit a significantly increased heat transfer rate during the initial impingement process. This implies potential for enhanced heat transfer designs to increase the contact frequency between droplets and the heated substrate.

4. Conclusion

By combining the 2c-PLIF and μPIV technologies, we obtain the quantitative velocity and temperature distributions of the droplet impingement process with high temporal and spatial resolution. With insights into droplet velocity fields, we demonstrate quantitatively that the boiling phenomena could enhance the internal mixing and viscous dissipation, hinders droplet recoiling from maximum spreading, and leads to a slower rebound for droplets within the contact boiling regime. Moreover, the direct temperature field measurements reveal a hot region with a spot-like shape in the spreading stage of droplets. This observation suggests that the thermal resistance beneath the droplet is not uniform. We also discover that the frequent contacts between droplet and the heated substrate

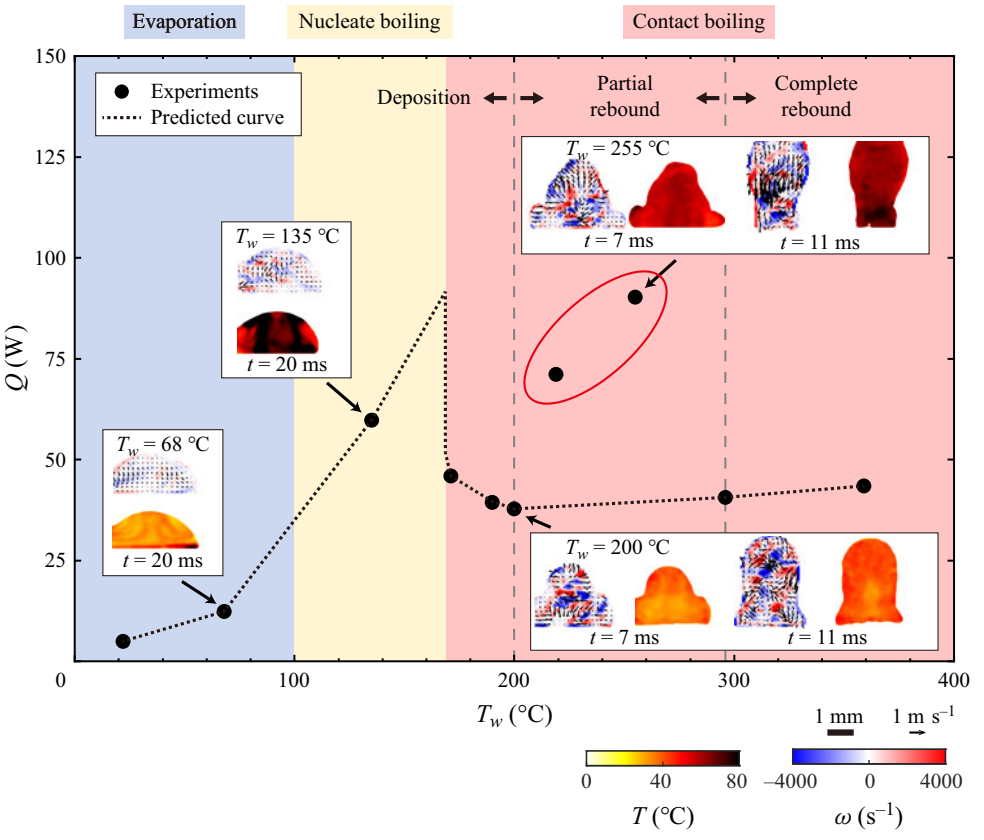

Figure 18. Droplet impingement heat transfer rate Q (black circles) at different wall temperatures. The black dashed line indicates the trend of heat transfer rate predicted from the droplet lifetime curve (figure 7). Boiling regimes can be separated into evaporation ($T_w < 100\,^{\circ}$C), nucleate boiling ($T_w = 100\,^{\circ}$C–$171\,^{\circ}$C) and contact boiling regimes ($T_w > 171\,^{\circ}$C). The grey dashed lines mark the transition wall temperatures $T_w = 200\,^{\circ}$C and $296\,^{\circ}$C of different droplet impingement outcomes: deposition, partial rebound and complete rebound. The velocity and temperature fields of droplets with typical boiling phenomena are shown in the figure (corresponding to four large symbols in the heat transfer rate curve).

can significantly enhance the heat transfer rate during the impinging process, despite the thermal resistance from the vapour layer.

Finally, our experimental methods have the potential to uncover additional detailed flow and heat transfer phenomena, as well as essential mechanisms underlying dynamic Leidenfrost droplets or other fundamental processes in droplet-impacting-based technologies in future works. The availability of simultaneous and resolved velocity and temperature field data, especially for problems involving temperature-gradient-induced flow and non-axisymmetric flow structures (Chen *et al.* 2016; Chakraborty, Chubynsky & Sprittles 2022), could greatly benefit the development of advanced numerical simulation or machine learning methods.

Supplementary material. Supplementary material is available at https://doi.org/10.1017/jfm.2024.751.

Acknowledgements. We thank the discussion from National Key Laboratory of Ramjet.

Funding. This work was supported by the National Natural Science Foundation of China (no. U2141250, no. 52225603).

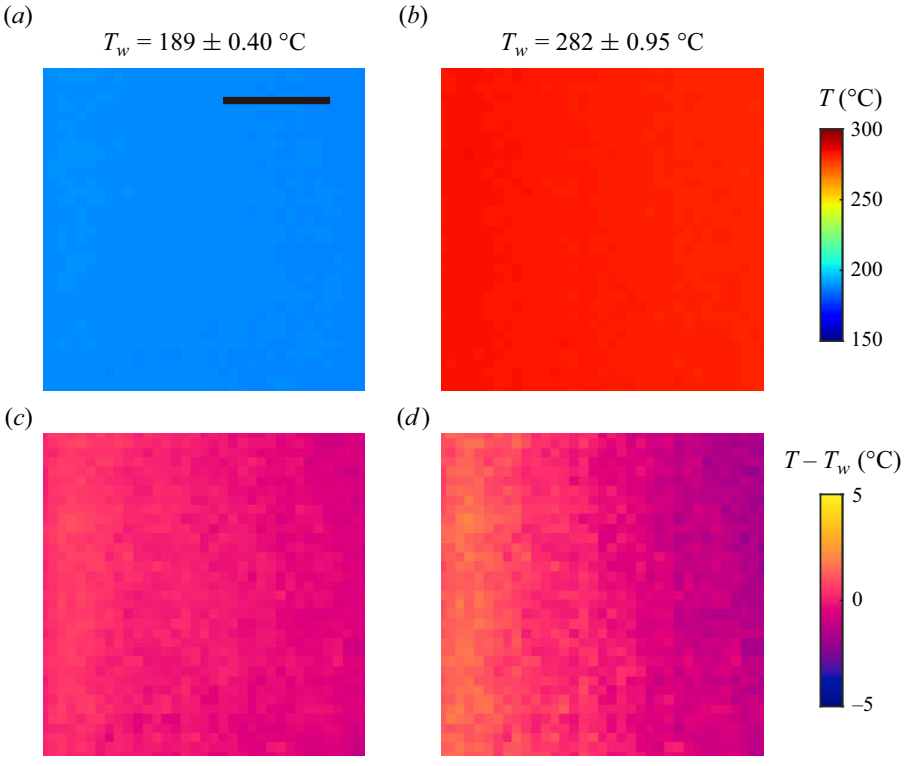

Figure 19. Two IR images of the heated substrates with wall temperatures (*a*) $T_w = 189\,^{\circ}\mathrm{C}$ and (*b*) $T_w = 282\,^{\circ}\mathrm{C}$. The temperature deviations are $0.40\,^{\circ}\mathrm{C}$ and $0.95\,^{\circ}\mathrm{C}$, respectively. Distributions of the temperature difference with wall temperatures (*c*) $T_w = 189\,^{\circ}\mathrm{C}$ and (*d*) $T_w = 282\,^{\circ}\mathrm{C}$. The black bar represents a length scale of 5 mm. The colour bars show the value of surface temperature distribution T for (*a*,*b*), and temperature difference distribution $T - T_w$ for (*c*,*d*).

Declaration of interests. The authors report no conflict of interest.

Author ORCIDs.
Ruina Xu https://orcid.org/0000-0001-8561-560X;
Xun Zhu https://orcid.org/0000-0002-5870-1921;
Peixue Jiang https://orcid.org/0000-0002-9777-8075.

Appendix. Temperature homogeneity of the heated substrate

The temperature homogeneity of the heated substrate was studied using IR imaging. The IR camera was placed above the heated substrate. The heating unit's configuration remained the same as in § 2.1. The silicon substrate was coated with an opaque and emissive black paint in the IR domain, making the emission from the substrate uniform, and reducing the reflection. In figure 19, we measure the temperature distribution of the heated silicon experimental substrate (area 15×15 mm^2) with wall temperature $T_w = 189\,^{\circ}\mathrm{C}$–$282\,^{\circ}\mathrm{C}$. The IR images show that the temperature fluctuation is less than $1\,^{\circ}\mathrm{C}$, which is relatively small compared to the wall temperature. Therefore, the effect of the temperature difference of the steadily heated substrate could be neglected.

References

Auliano, M., Auliano, D., Fernandino, M., Zhang, P. & Dorao, C.A. 2018 Water droplet dynamics on a heated nanowire surface. *Appl. Phys. Lett.* **113** (25), 253703.

Benther, J.D., Pelaez-Restrepo, J.D., Stanley, C. & Rosengarten, G. 2021 Heat transfer during multiple droplet impingement and spray cooling: review and prospects for enhanced surfaces. *Intl J. Heat Mass Transfer* **178**, 121587.

Bouillant, A., Mouterde, T., Bourrianne, P., Lagarde, A., Clanet, C. & Quéré, D. 2018 Leidenfrost wheels. *Nat. Phys.* **14** (12), 1188–1192.

Breitenbach, J., Roisman, I.V. & Tropea, C. 2017 Heat transfer in the film boiling regime: single drop impact and spray cooling. *Intl J. Heat Mass Transfer* **110**, 34–42.

Castanet, G., Caballina, O., Chaze, W., Collignon, R. & Lemoine, F. 2020 The Leidenfrost transition of water droplets impinging onto a superheated surface. *Intl J. Heat Mass Transfer* **160**, 120126.

Castanet, G., Caballina, O. & Lemoine, F. 2015 Drop spreading at the impact in the Leidenfrost boiling. *Phys. Fluids* **27** (6), 063302.

Castanet, G., Chaze, W., Caballina, O., Collignon, R. & Lemoine, F. 2018 Transient evolution of the heat transfer and the vapor film thickness at the drop impact in the regime of film boiling. *Phys. Fluids* **30** (12), 122109.

Cazabat, A.-M. & Guena, G. 2010 Evaporation of macroscopic sessile droplets. *Soft Matt.* **6** (12), 2591–2612.

Chakraborty, I., Chubynsky, M.V. & Sprittles, J.E. 2022 Computational modelling of Leidenfrost drops. *J. Fluid Mech.* **936**, A12.

Chaze, W., Caballina, O., Castanet, G. & Lemoine, F. 2016 The saturation of the fluorescence and its consequences for laser-induced fluorescence thermometry in liquid flows. *Exp. Fluids* **57** (4), 58.

Chaze, W., Caballina, O., Castanet, G. & Lemoine, F. 2017 Spatially and temporally resolved measurements of the temperature inside droplets impinging on a hot solid surface. *Exp. Fluids* **58** (8), 96.

Chen, J., Zhang, Z., Xu, R., Ouyang, X. & Jiang, P. 2016 Numerical investigation of the flow dynamics and evaporative cooling of water droplets impinging onto heated surfaces: an effective approach to identify spray cooling mechanisms. *Langmuir* **32** (36), 9135–9155.

Chen, K., Xu, R.-N. & Jiang, P.-X. 2021 Experimental study of jet impingement boiling cooling with CO_2 at subcritical pressures and comparisons with at supercritical pressures. *Intl J. Heat Mass Transfer* **165**, 120605.

Christy, J.R.E., Hamamoto, Y. & Sefiane, K. 2011 Flow transition within an evaporating binary mixture sessile drop. *Phys. Rev. Lett.* **106** (20), 205701.

Cummings, D.L. & Blackburn, D.A. 1991 Oscillations of magnetically levitated aspherical droplets. *J. Fluid Mech.* **224**, 395–416.

Dash, S., Chandramohan, A., Weibel, J.A. & Garimella, S.V. 2014 Buoyancy-induced on-the-spot mixing in droplets evaporating on nonwetting surfaces. *Phys. Rev.* E **90**, 062407.

Diddens, C., Li, Y. & Lohse, D. 2021 Competing Marangoni and Rayleigh convection in evaporating binary droplets. *J. Fluid Mech.* **914**, A23.

Efstratiou, M., Christy, J. & Sefiane, K. 2020 Crystallization-driven flows within evaporating aqueous saline droplets. *Langmuir* **36** (18), 4995–5002.

Eggers, J., Fontelos, M.A., Josserand, C. & Zaleski, S. 2010 Drop dynamics after impact on a solid wall: theory and simulations. *Phys. Fluids* **22** (6), 062101.

Erkan, N. 2019 Full-field spreading velocity measurement inside droplets impinging on a dry solid-heated surface. *Exp. Fluids* **60** (5), 88.

Graeber, G., Regulagadda, K., Hodel, P., Küttel, C., Landolf, D., Schutzius, T.M. & Poulikakos, D. 2021 Leidenfrost droplet trampolining. *Nat. Commun.* **12** (1), 1727.

Gultekin, A., Erkan, N., Colak, U. & Suzuki, S. 2020 PIV measurement inside single and double droplet interaction on a solid surface. *Exp. Fluids* **61** (10), 218.

Hamamoto, Y., Christy, J.R.E. & Sefiane, K. 2011 Order-of-magnitude increase in flow velocity driven by mass conservation during the evaporation of sessile drops. *Phys. Rev.* E **83** (5), 051602.

Huang, C.-T., Lo, C.-W. & Lu, M.-C. 2022 Reducing contact time of droplets impacting superheated hydrophobic surfaces. *Small* **18** (13), 2106704.

Kang, K.H., Lee, S.J., Lee, C.M. & Kang, I.S. 2004 Quantitative visualization of flow inside an evaporating droplet using the ray tracing method. *Meas. Sci. Technol.* **15** (6), 1104.

Lamb, H. 1924 *Hydrodynamics*. Cambridge University Press.

Lastakowski, H., Boyer, F., Biance, A.-L., Pirat, C. & Ybert, C. 2014 Bridging local to global dynamics of drop impact onto solid substrates. *J. Fluid Mech.* **747**, 103–118.

LI, Y., DIDDENS, C., LV, P., WIJSHOFF, H., VERSLUIS, M. & LOHSE, D. 2019 Gravitational effect in evaporating binary microdroplets. *Phys. Rev. Lett.* **122**, 114501.

LIANG, G., CHEN, Y., CHEN, L. & SHEN, S. 2019 Maximum spreading for liquid drop impacting on solid surface. *Ind. Engng Chem. Res.* **58** (23), 10053–10063.

LIANG, G. & MUDAWAR, I. 2017 Review of drop impact on heated walls. *Intl J. Heat Mass Transfer* **106**, 103–126.

LIU, L., ZHANG, Y., CAI, G. & TSAI, P.A. 2022 High-speed dynamics and temperature variation during drop impact on a heated surface. *Intl J. Heat Mass Transfer* **189**, 122710.

LOHSE, D. 2022 Fundamental fluid dynamics challenges in inkjet printing. *Annu. Rev. Fluid Mech.* **54** (1), 349–382.

LYU, S., MATHAI, V., WANG, Y., SOBAC, B., COLINET, P., LOHSE, D. & SUN, C. 2019 Final fate of a Leidenfrost droplet: explosion or takeoff. *Sci. Adv.* **5** (5), eaav8081.

LYU, S., TAN, H., WAKATA, Y., YANG, X., LAW, C.K., LOHSE, D. & SUN, C. 2021 On explosive boiling of a multicomponent Leidenfrost drop. *Proc. Natl Acad. Sci. USA* **118**, e2016107118.

MARTIN, H. 1977 Heat and mass transfer between impinging gas jets and solid surfaces. In *Advances in Heat Transfer* (ed. J.P. Hartnett & T.F. Irvine Jr), vol. 13, pp. 1–60. Elsevier.

MISYURA, S.Y., MOROZOV, V.S., VOLKOV, R.S. & VYSOKOMORNAYA, O.V. 2019 Temperature and velocity fields inside a hanging droplet of a salt solution at its streamlining by a high-temperature air flow. *Intl J. Heat Mass Transfer* **129**, 367–379.

MOREIRA, A.L.N., MOITA, A.S. & PANÃO, M.R. 2010 Advances and challenges in explaining fuel spray impingement: how much of single droplet impact research is useful? *Prog. Energy Combust. Sci.* **36** (5), 554–580.

RAFFEL, M., WILLERT, C.E., SCARANO, F., KÄHLER, C.J., WERELEY, S.T. & KOMPENHANS, J. 2018 *Particle Image Velocimetry: A Practical Guide*. Springer.

RICHARD, D., CLANET, C. & QUÉRÉ, D. 2002 Contact time of a bouncing drop. *Nature* **417** (6891), 811.

RIOBOO, R., MARENGO, M. & TROPEA, C. 2002 Time evolution of liquid drop impact onto solid, dry surfaces. *Exp. Fluids* **33** (1), 112–124.

ROISMAN, I.V., BERBEROVI, E. & TROPEA, C. 2009 Inertia dominated drop collisions. I. On the universal flow in the lamella. *Phys. Fluids* **21** (5), 052103.

ROISMAN, I.V., BREITENBACH, J. & TROPEA, C. 2018 Thermal atomisation of a liquid drop after impact onto a hot substrate. *J. Fluid Mech.* **842**, 87–101.

SANJAY, V., CHANTELOT, P. & LOHSE, D. 2023 When does an impacting drop stop bouncing? *J. Fluid Mech.* **958**, A26.

SANTIAGO, J.G., WERELEY, S.T., MEINHART, C.D., BEEBE, D.J. & ADRIAN, R.J. 1998 A particle image velocimetry system for microfluidics. *Exp. Fluids* **25** (4), 316–319.

SCIACCHITANO, A., NEAL, D.R., SMITH, B.L., WARNER, S.O., VLACHOS, P.P., WIENEKE, B. & SCARANO, F. 2015 Collaborative framework for PIV uncertainty quantification: comparative assessment of methods. *Meas. Sci. Technol.* **26** (7), 074004.

SHIRI, S. & BIRD, J.C. 2017 Heat exchange between a bouncing drop and a superhydrophobic substrate. *Proc. Natl Acad. Sci. USA* **114** (27), 6930–6935.

SHIROTA, M., VAN LIMBEEK, M.A.J., SUN, C., PROSPERETTI, A. & LOHSE, D. 2016 Dynamic Leidenfrost effect: relevant time and length scales. *Phys. Rev. Lett.* **116**, 064501.

STAAT, H.J.J., TRAN, T., GEERDINK, B., RIBOUX, G., SUN, C., GORDILLO, J.M. & LOHSE, D. 2015 Phase diagram for droplet impact on superheated surfaces. *J. Fluid Mech.* **779**, R3.

STONE, H.A., STROOCK, A.D. & AJDARI, A. 2004 Engineering flows in small devices: microfluidics toward a lab-on-a-chip. *Annu. Rev. Fluid Mech.* **36**, 381–411.

TEODORI, E., PONTES, P., MOITA, A.S. & MOREIRA, A.L.N. 2018 Thermographic analysis of interfacial heat transfer mechanisms on droplet/wall interactions with high temporal and spatial resolution. *Exp. Therm. Fluid Sci.* **96**, 284–294.

TRAN, T., STAAT, H.J.J., PROSPERETTI, A., SUN, C. & LOHSE, D. 2012 Drop impact on superheated surfaces. *Phys. Rev. Lett.* **108**, 036101.

VOLKOV, R.S. & STRIZHAK, P.A. 2021 Using planar laser induced fluorescence and micro particle image velocimetry to study the heating of a droplet with different tracers and schemes of attaching it on a holder. *Intl J. Therm. Sci.* **159**, 106603.

VOULGAROPOULOS, V., AGUIAR, G.M., MARKIDES, C.N. & BUCCI, M. 2022 Simultaneous laser-induced fluorescence, particle image velocimetry and infrared thermography for the investigation of the flow and heat transfer characteristics of nucleating vapour bubbles. *Intl J. Heat Mass Transfer* **187**, 122525.

WANG, A.-B., LIN, C.-H. & CHENG, C.-C. 2005 Pattern analysis of a single droplet impinging onto a heated plate. *Heat Transfer Asian Res.* **34** (8), 579–594.

WANG, Z., OREJON, D., TAKATA, Y. & SEFIANE, K. 2022 Wetting and evaporation of multicomponent droplets. *Phys. Rep.* **960**, 1–37.

WILDEMAN, S., VISSER, C.W., SUN, C. & LOHSE, D. 2016 On the spreading of impacting drops. *J. Fluid Mech.* **805**, 636–655.

XU, R., WANG, G. & JIANG, P. 2021 Spray cooling on enhanced surfaces: a review of the progress and mechanisms. *J. Electron. Packag.* **144** (1), 010802.

YANG, J., LI, Y., WANG, D., FAN, Y., MA, Y., YU, F., GUO, J., CHEN, L., WANG, Z. & DENG, X. 2023 A standing Leidenfrost drop with Sufi whirling. *Proc. Natl Acad. Sci. USA* **120** (32), e2305567120.

YARIN, A.L. & WEISS, D.A. 1995 Impact of drops on solid surfaces: self-similar capillary waves, and splashing as a new type of kinematic discontinuity. *J. Fluid Mech.* **283**, 141–173.

YIM, E., BOUILLANT, A. & GALLAIRE, F. 2021 Buoyancy-driven convection of droplets on hot nonwetting surfaces. *Phys. Rev.* E **103**, 053105.

YIM, E., BOUILLANT, A., QUÉRÉ, D. & GALLAIRE, F. 2022 Leidenfrost flows: instabilities and symmetry breakings. *Flow* **2**, E18.

YU, X., ZHANG, Y., HU, R. & LUO, X. 2021 Water droplet bouncing dynamics. *Nano Energy* **81**, 105647.